Field flattening concepts for linac cavities of the cross-bar *H* type

Ali M. Almomani*
Physics Department, Faculty of Science, Yarmouk University, 211-63 Irbid, Jordan

Ulrich Ratzinger
Institute for Applied Physics, Goethe University, Max-von-Laue Straße 1, 60438 Frankfurt am Main, Germany and Helmholtz Forschungsakademie Hessen für FAIR (HFHF), GSI Helmholtzzentrum für Schwerionenforschung, Campus Frankfurt, Frankfurt, Germany

(Received 25 October 2023; accepted 18 March 2024; published 5 April 2024)

The development of cross-bar H-type cavities (CH-DTL, H_{21} mode) is ongoing to improve the technology of this attractive type of drift tube linac (DTL). In comparison with the conventional DTL, the H-type cavities can reach a higher effective field gradient and are competitive in shunt impedance at an energy range up to 100 A MeV. H-mode DTL's profit in shunt impedance additionally when applying the KONUS beam dynamics. They are in use at research laboratories as well as at hospitals. This paper describes a new concept to approach the zero mode in CH-type cavities, by extending the cavity diameter at the tank ends in combination with tilted drift tube stems. RFQs of the four-vane type are operated as well in the H_{210} mode and the strategy for voltage flattening can be partly applied there too if conventional vane undercuts are causing problems. Up to around 35 MeV, it is attractive to integrate one or more triplet lenses into each cavity, as one KONUS section is relatively short and would not exploit the full rf power of 3 MW klystrons which are available above 300 MHz. Such a cavity is denoted as a coupled CH-cavity CCH. Three possible arrangements of those internal triplet lenses are discussed and are compared to each other. The operating modes as well as higher modes are then compared with a lens-free CH cavity, where the lens position was filled by ordinary drift tubes. As a result, it is shown that the rf behavior and resonance frequency for the higher harmonics of the frequency band are very similar for all four investigated arrays. This means, that the tuning behavior of the CCH cavity can be simply deduced from the lens-free CH cavity by replacing an even number of ordinary drift tubes ($n\beta\lambda$) with a lens-containing drift tube with adequate length and large outer diameter. This large drift tube itself oscillates like an Alvarez-type drift tube. rf simulations on a 30-gap CH cavity show that the reduction in shunt impedance is about 10% when installing a lens with length 2 beta lambda.

DOI: 10.1103/PhysRevAccelBeams.27.040101

I. INTRODUCTION

The activities in linear ion accelerators aim at the development of high intensity, high energy, low, and high duty factor accelerators for proton and ion beams. Those accelerators have to fulfill the demands of fundamental and applied sciences. For pulsed high current linacs, room temperature solutions are chosen at least up to beam energies around 100 MeV. Multigap cavities are used due to their high efficiency. The traditional solution is the Alvarez-type DTL (E_{010} mode), while H-type DTLs were established first for heavy ion acceleration as IH structures in the H_{110} mode [1,2]. Only during the last years with the development of the CH-DTL [3] and applying the H_{210} mode, these structures also offer an option for light ion and proton acceleration [4,5].

In conventional Alvarez-type drift tube linacs of the $\beta\lambda$ type, the mechanical gap lengths sum up to about 25% of the full cavity length. This kind of cavity is operated in the E_{010} mode and shows high stored field energies. If electromagnetic quadrupoles are used inside each drift tube, the outer tube diameters have to be rather large. These geometrical necessities with parallel drift tube end faces determine the maximum effective voltage gain per meter. Recently, with using permanent-magnetic quadrupoles for proton DTLs of that type, the situation with respect to shunt impedance and maximum voltage gain has improved [6–8].

The H-type structures can be an alternative to the conventional drift tube linacs at energies up to around 100 AMeV. H-type structures are of the $\beta\lambda/2$-type where the gap lengths fill about 50% along the beam axis.

*Corresponding author: ali.almomani@yu.edu.jo

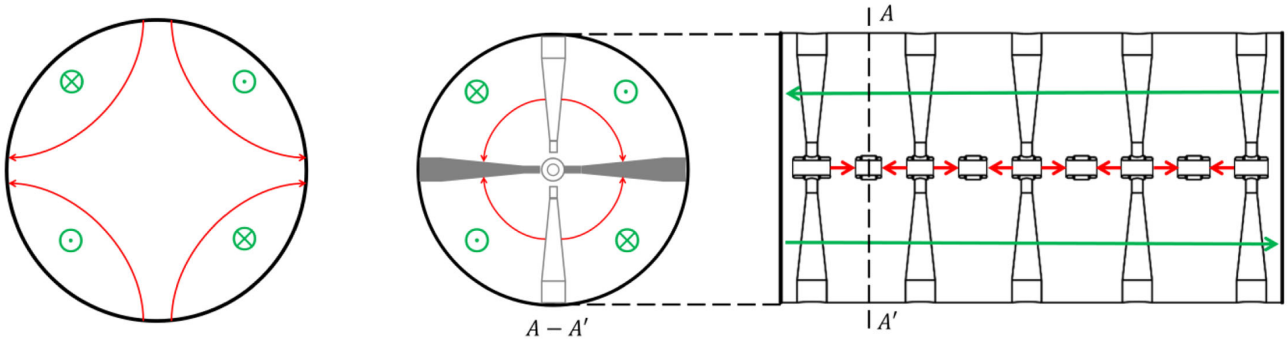

FIG. 1. Electric (in red) and magnetic (in green) field lines for the H_{211} mode in an empty cavity (left) and in a loaded CH cavity (right).

This allows about a factor of 2 more voltage gain per length when compared to the conventional DTL. Moreover, it was demonstrated that the slim drift tube surfaces can stand very high surface fields [9]. Medical synchrotron injectors at several hospitals around the world use IH-DTL cavities with an average effective field gain of 7.2 MV/m along the first drift tube section. The dark currents at these field levels are negligible [10]. This robustness of thin-walled drift tubes against sparking is essential for H-type structures, as their shunt impedance profits directly from a low capacitive load. Optionally, the combination of cavity-internal quadrupole triplets with slim drift tube sections by the KONUS beam dynamics allows to increase both—the particle acceleration and efficiency of these structures [2,11]. Permanent-magnetic quadrupoles in case of H-type proton linacs should be a future option also in case of H- type linacs and this was investigated by [12,13].

One can compare the CERN-Linac4-DTL2 cavity (E_{010} mode, permanent magnetic quadrupoles) with the CCH2 cavity of the GSI/FAIR-proton linac: DTL2 is 5.2 m long and accelerates from 9.8 to 25 MeV. The power-tested CCH2 prototype cavity is 2.9 m long and accelerates from 9.9 to 21.1 MeV. About 40% higher field levels above that design level were indeed reached at the GSI test stand [14]. This underlines the high field gain capabilities of the H-type structures. In this energy range, both cavity types reach an effective shunt impedance of around 53 MΩ/m.

The H-type cavities are characterized by the directions of the rf magnetic field lines, which are parallel and anti-parallel with respect to the beam axis and turn around at the cavity ends to form closed loops [15]. The electric and magnetic field distributions for the H_{211} mode in pillbox cavities are shown in Fig. 1, left side.

Only the transverse electric field component exists in a pillbox cavity, while the accelerating longitudinal component is created by introducing a $\beta\lambda/2$-type drift tube structure along the beam axis, connected with the cavity wall by stems. The H-type drift tube linacs are realized either as IH structures (H_{110} mode) or as CH structures (H_{210} mode).

At the low-beta range, the Interdigital "IH-DTL" can be used to accelerate particles up to $\beta \approx 0.25$ [16]. Recently—with additive manufacturing techniques—frequencies above 300 MHz can be realized [17], shifting the β limit to around 0.3.

Instead, at higher frequencies and beam velocities, one can use the H_{210} mode. The cavity diameters at a given frequency are then larger, as the inductance per length is reduced [15]. These cavities profit as well from additive manufacturing [18]. As a consequence, to extend the H-type cavities to higher energies in the range up to 100 A MeV and beyond, the CH-DTL has been under development since several years at IAP, Frankfurt University, and at GSI, Darmstadt [19,20]. Room temperature CH cavities have been investigated also in LANL, Los Alamos, and at FNL, Batavia [21,22].

An important topic for efficient multigap acceleration is the generation of a zero mode. In H-mode cavities, this mode does not exist unless an accelerating structure is installed—like in four-vane-RFQs or in IH-DTLs: In both cases undercuts in the vanes and girders, respectively, are used to establish the zero mode. In CH-DTLs, the stems are in most cases directly connected to the cylindrical cavity walls. Therefore, a different way of getting the zero mode is needed. Reference [3] and the left plot in Fig. 2 show the resonant tuning of the end cells by long half-drift tubes mounted on the cavity end walls. One can try to use this space partly for housing the intertank quadrupole lens. However, it hampers linac installation and services. An alternative concept is shown in chapter II of this publication.

The KONUS beam dynamics enables only relatively short, lens-free accelerating sections at the low energy end. However, due to the available 3-MW klystrons, one likes to increase the number of gaps in each cavity to exploit that power. The FAIR proton linac relies on this concept in the first three CCH cavities. As an example, Fig. 2 on the right shows an early 3D model study of the second coupled cavity of the FAIR proton linac [23]. Cavity internal lenses optimize the beam quality, as the drifts between accelerating sections are as short as possible by applying the technique of coupling cells.

In this paper, the coupling mechanism of two CH sections by a large drift tube will be investigated in

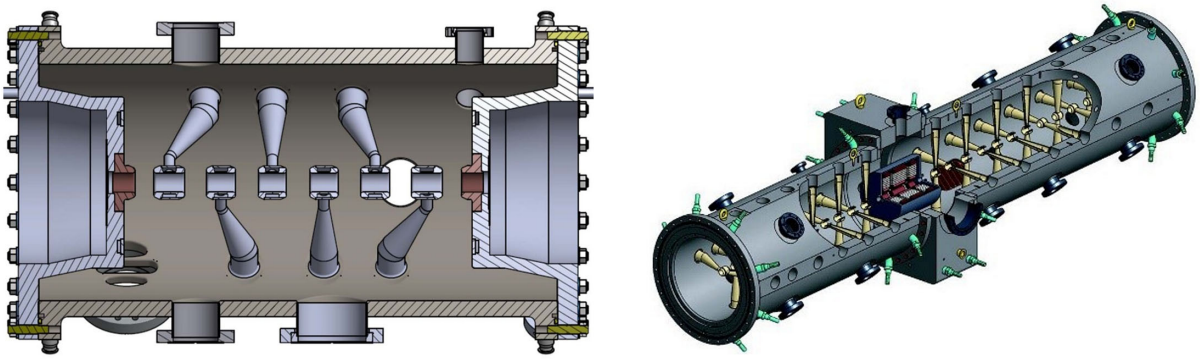

FIG. 2. View into one half of the CH-DTL [20] (left) and 3D view on a CCH-DTL with a quadrupole triplet containing coupling cell (right, 3D view from Ref. [23]).

detail. It should help to apply that CCH technology in future projects. A typical CCH cavity is specified in detail and the coupling fields around the large drift tube are explained. The similarity between three different coupling arrays will be justified by the identical higher order mode spectrum. All field simulations were performed with CST studio suite [24].

II. END CAPS WITH EXTENDED DIAMETER TO ESTABLISH THE H_{210} MODE

A. Drift tube cavity of the CH type

A new technique to achieve a flat voltage distribution in CH cavities is an increased cavity diameter at the tank ends, accompanied by an inclined last stem, as shown in Fig. 3. The intertank lenses may still reach a bit into the cavity end plane but give no more a major contribution to the voltage flattening. The method was applied at all six cavities of the FAIR p-linac for the first time [25]. The technical realization of those radial extensions was realized with low extra efforts at the joints between cylindrical tanks and end lids

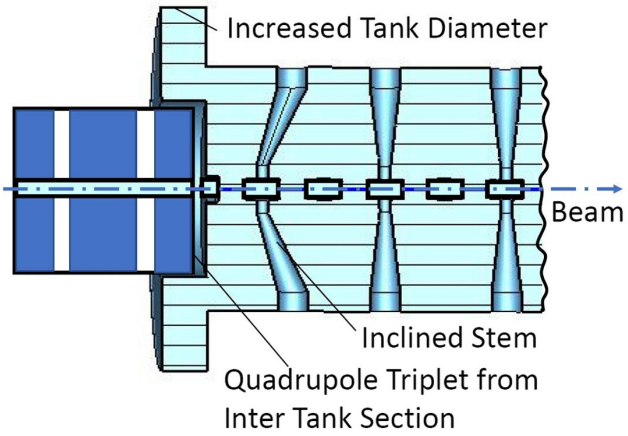

FIG. 3. End geometry of a CH cavity with quadrupole triplet from an intertank section. The radial tank extensions and the inclined stems at both tank ends allow for a zero-mode operation—H_{210}.

[18]. Figure 3 shows one cavity end region of a 30-gap CH cavity with equidistant gaps. The gap voltage distribution along one-half of the cavity in dependence on the cavity diameter choice at the tank ends is shown in Fig. 4(a). Figure 4(b) shows the variation of the length L of the radially extended ends.

As a consequence, the half-drift tubes mounted at the cavity end walls can be chosen as short as mechanically reasonable (in contrast to the former techniques described in [3] and shown in Fig. 2, left side). While minimizing the total length of intersections between two CH cavities for beam dynamics reasons (to keep the bunches short), the mechanical layout and the accessibility to the components of those sections were considerably relaxed by that new cavity design. The shorter tank length results in an improved shunt impedance. Figure 4 explains quantitatively the influence of the two geometric parameters R_e and L on the gap voltage distribution. The cavity with 30 gaps from Fig. 8 was used for that simulation, with the first and last stems of the cavity kept inclined [see Fig. 5(a)] at a constant value. As a result, both geometry parameters can be used very efficiently for changing the gap voltage distribution.

The third highly efficient parameter for zero-mode tuning of a CH cavity is the inclination Δl (see Fig. 5) of the last stem. The balance between Δl, the diameter ratio R_E/R_C, and length L can be chosen accordingly, depending on the cell length and mechanical restrictions like the vacuum sealing concept, the realization of cooling channels, etc. The zero mode can be achieved within a wide three-parameter space.

The efficiency in flattening the voltage distribution and the influence on the effective shunt impedance can be seen in Tables I–III, corresponding to the cases plotted in Figs. 4 and 5. A flatness parameter F is defined to compare different tuning cases:

$$F = \frac{\sum V_i}{N V_{\max}}, \tag{1}$$

where N is the total number of cavity gaps.

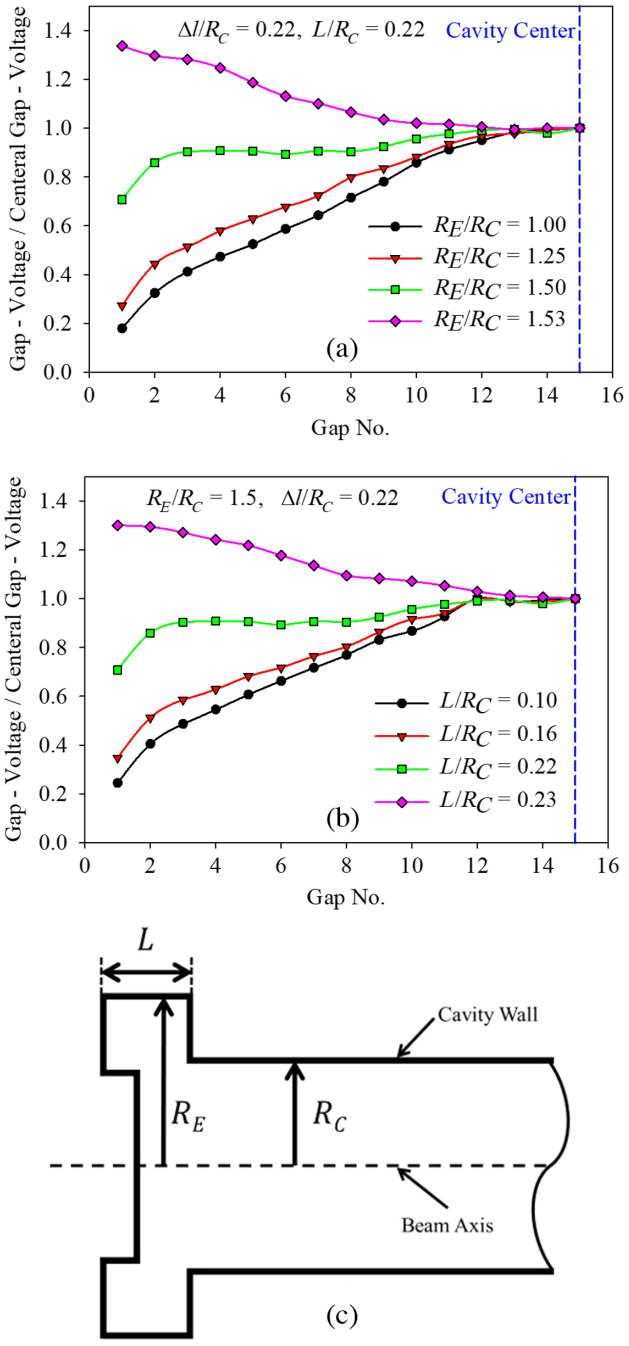

FIG. 4. (a) Influence of the R_E/R_C ratio on the gap voltage distribution along a 30-gap CH structure, L is kept constant at a value $L/R_C = 0.22$. (b) Dependence of the gap voltage distribution on L at a fixed $R_E/R_C = 1.5$. (c) Cavity end shape with indication of the key parameters. L is varied by shifting the inner wall (right side). The tank length is kept constant.

There is no advantage in shunt impedance when pushing the outermost gaps further up toward F against 1.0, as these end regions are more lossy than the main structure. In this study, an optimum was found for $R_E/R_C = 1.5$, $L/R_C = 0.22$, and $\Delta l/R_C = 0.22$, corresponding to $F = 0.85$.

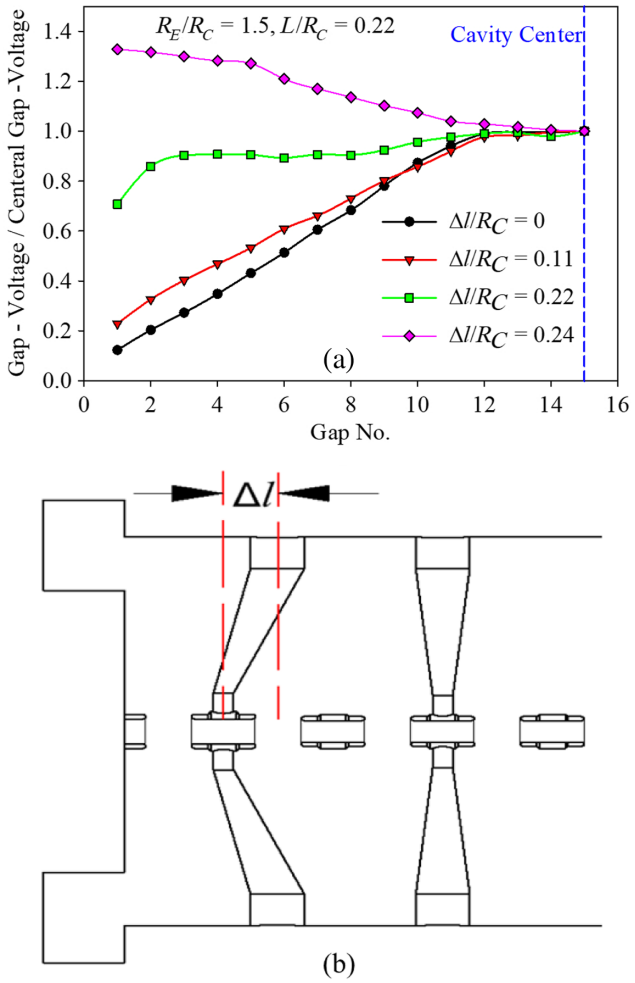

FIG. 5. (a) Influence of the last stem inclination Δl on the gap voltage distribution. (b) Inclined last stem with definition of Δl.

B. RFQ cavity of the four-vane type

The same end-geometry concept can be applied to four-vane-RFQs (H_{210} mode) if the classical undercuts have to be avoided or might cause technical difficulties. One reason against undercuts can be water-cooling problems in case of high duty factors. Another reason may be the overhang problem [26] when applying the additive manufacturing process for vane production [27].

TABLE I. Effect of the R_E/R_C ratio on the cavity parameters F, frequency, Z_{eff}, and Q value for the 30-gap cavity in Fig. 8. Parameters $\Delta l/R_C = 0.22$ and $L/R_C = 0.22$ are kept constant, see Fig. 4(a).

R_E/R_C	1	1.25	1.50	1.53
F	0.67	0.70	0.85	0.75
Frequency (MHz)	325.12	325.06	324.69	324.50
Z_{eff} (MΩ/m)	48.83	49.53	58.59	52.2
Q value	13 654	13 916	14 386	14 028

TABLE II. Effect of the L/R_C ratio on the cavity parameters for $\Delta l/R_C = 0.22$ and $R_E/R_C = 1.5$, see Fig. 4(b).

L/R_C	0.10	0.16	0.22	0.23
F	0.73	0.79	0.85	0.76
Frequency (MHz)	325.10	325.00	324.69	324.53
Z_{eff} (MΩ/m)	51.16	53.21	58.59	51.72
Q value	13 561	13 800	14 386	13 369

TABLE III. Effect of the parameter Δl on the cavity parameters for $L/R_C = 0.22$, $R_E/R_C = 1.5$, see Fig. 5(a).

$\Delta l/R_C$	0	0.11	0.22	0.24
F	0.58	0.65	0.85	0.77
Frequency (MHz)	324.32	325.16	324.69	324.48
Z_{eff} (MΩ/m)	39.59	45.32	58.59	53.49
Q value	12 599	12 634	14 386	14 007

A comparison between the undercut depth L_U and the corresponding parameters R_E and L can be found below. A four-vane-RFQ with tank radius R_C and alternative end geometries as sketched in Fig. 6 was investigated, with vane-tip parameters $\rho/R_C = 0.0248$, $R_0/R_C = 0.0095$. ρ and R_0 denote the vane-tip curvature and the mean aperture radius of the RFQ, respectively. The relative cavity length was $L_C/R_C = 19$.

Two RFQ designs with extended cavity ends and one design with undercuts are compared with each other in Table IV. All three cases show a flat voltage distribution along the full vane length with $\Delta V/V \leq \pm 6\%$. A comparison of the two alternative layouts with extended radii shows a large influence of L on R_E. Large R_E/R_C ratios are only recommended at high enough frequencies with small tank radii R_C.

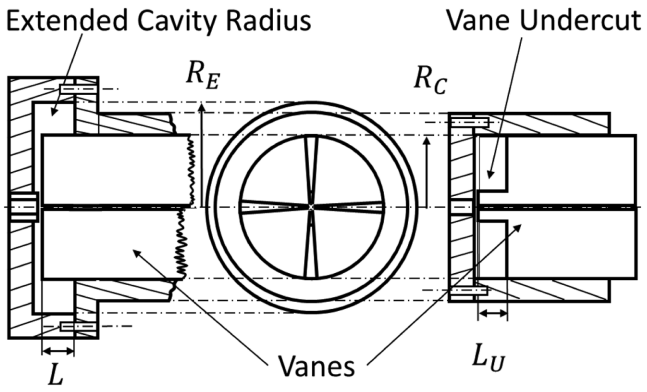

FIG. 6. Comparison of a classical undercut geometry (right) with the concept of an extended cavity radius at the end caps (left). The center of the plot shows the RFQ cross-sectional view.

TABLE IV. Comparison of three parameter sets that generate a zero mode.

Type	L_U/R_C	R_E/R_C	L/R_C	Q/Q_U
Undercut	0.457	1	0	1.00
Extended radius	0	1.476	0.476	1.01
Extended radius	0	1.810	0.429	1.00

III. CCH CAVITY INVESTIGATIONS WITH RESPECT TO THE COUPLING CELL

It is investigated, how a cavity with an internal big drift tube can be described from the rf point of view. One early approach was to consider such an array as three coupled oscillators—the two CH drift tube sections and the lens [3]. However, the coupling cell (compare Fig. 7) is completely different from the accelerating sections before and behind. Moreover, sections one and two show their own mode spectrum, and the coupling between their $\beta\lambda/2$ cells ($k \cong 0.5$, see below) is not hard enough to be neglected. For an equivalent model to describe the coupling between CH sections and the coupling cell, the capacitive and inductive components would have to be included.

Finally, an easy approach was found how to design the two CH drift tube sections to be ready for coupling by the big drift tube and getting a flat voltage distribution.

As the process is described by a kind of recipe, an example cavity is defined to explain the concept.

The CCH cavity has 27 gaps in total and the energy profile is from 9.9 to 21.1 MeV, see Fig. 7 and Table V. The first accelerating section has 13 gaps and the second one has 14 gaps. The coupling cell corresponds to a length of $2\beta\lambda$. Table V shows the simulated key parameters of this cavity. Figure 7 shows a sketch of the cavity with horizontal and vertical cuts and gives the main dimensions.

This array of drift tubes for acceleration and transverse focusing fulfills the beam dynamics requests. The rf power needs including a 100 mA beam load are fitting to a 3 MW klystron.

For rf tuning of such a cavity, the following concept is recommended: (1) Replace the coupling lens with ordinary drift tubes filling the space: A coupling cell of length $N\beta\lambda$ is replaced by $2N$ drift tubes. This results in a standard CH configuration. (2) Perform the end-cell tuning by the method as described in chapter II. A. (3) Insert the coupling cell with its specified length and tune the cavity radius around the lens slightly to achieve the zero mode, now for the requested CCH cavity.

This concept is now demonstrated step by step.

A. Corresponding CH structure with drift tubes in section 3

A drift tube structure with a constant-beta profile is used now to show the coupling topic in a transparent manner. The simplified CH structure to develop the CCH cavity is

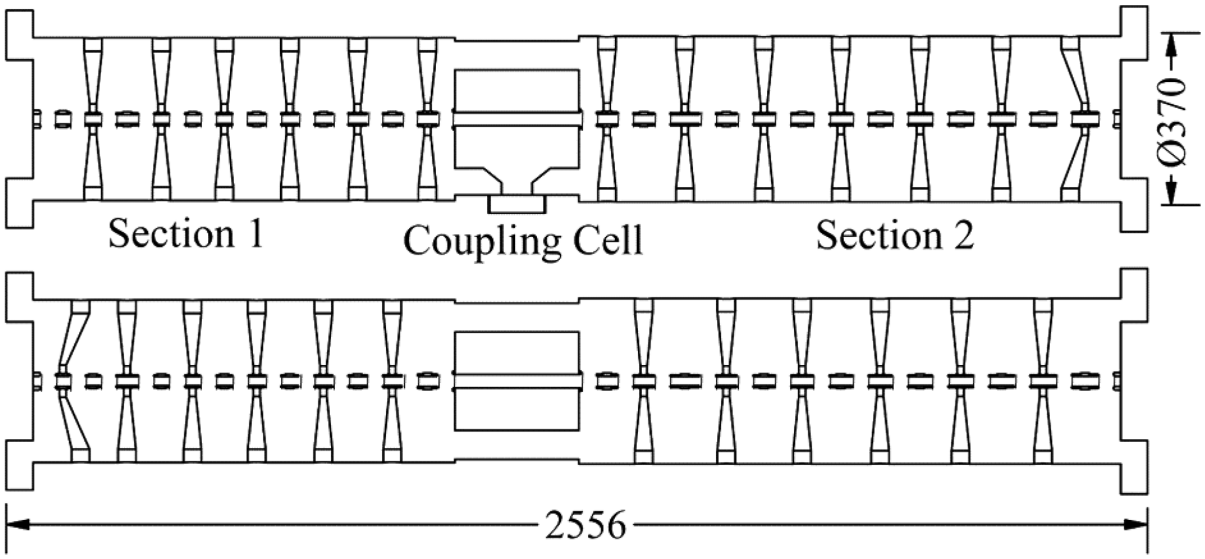

FIG. 7. Horizontal and vertical cuts of a 325.2 MHz CCH cavity showing the main dimensions. The proton acceleration is from 9.9 to 21.1 MeV. The radial tank extensions at the cavity ends and the inclined stems at the ends as explained in chapter II. A are also visible.

displayed in Fig. 8. The lens from Fig. 7 was replaced by four drift tubes of a $\beta\lambda/2$ structure now called section 3. The stem orientation of section 2 was changed by 90° due to the chosen coupling arrangement in that case (compare Fig. 13(a) and chapter III. B).

The mode spectrum of this CH configuration corresponds to 30 coupled cells, being equal to the number of gaps. The mode spectrum for a multicell structure with N cells and single-cell frequency ω_0 is given by [1]

$$\Omega_l = \frac{\omega_0}{\sqrt{1 + k\,\cos(\frac{\pi l}{N-1})}}, \qquad l = 0, 1, 2, \ldots N-1 \tag{2}$$

From the simulated values for Ω_0 and Ω_{N-1}, one can derive the coupling factor k via

$$\frac{\Omega_{N-1}^2}{\Omega_0^2} \equiv R = \frac{1+k}{1-k} \tag{3}$$

TABLE V. Main parameters of the investigated CCH cavity.

Number of gaps	27(13 + 14)
Design frequency (MHz)	325.224
Voltage gain (MV)	11.2
Eff. accel. length (mm)	2556
Power loss (MW)	1.04
Z_{eff} (MΩ/m)	53.2
Q_0 value	14 200
Drift tube aperture (mm)	20
Lens aperture (mm)	30
Lens outer diameter (mm)	220
Lens cell length	$2\beta\lambda$
Bandwidth (kHz)	22.9

$$k = \frac{R-1}{R+1}. \tag{4}$$

For k one gets from Eqs. (2) and (4)

$$\omega_0 = \Omega_0\sqrt{(1+k)}. \tag{5}$$

By comparison with an MWS-CST simulation [24] on the 30-cell CH structure, one gets the extreme values $\Omega_0 = 2\pi \cdot 324.743$ MHz and $\Omega_{29} = 2\pi \cdot 577.57$ MHz, resulting in

$$R = 3.163, \qquad k = 0.52, \qquad \omega_0 = 2\pi \cdot 400.32 \text{ MHz}. \tag{6}$$

The comparison between the mode spectrum from Eq. (2) and the simulation of the CH cavity is shown in Fig. 9. While the lower modes are the well-known spatial harmonics H_{21l} of the H_{21} mode, the higher modes are getting quite bizarre. This characteristic is an identical field orientation of a steadily increasing number of neighbored gaps, but modes are still showing electrical net currents along stems in contrast to E modes. By comparison of the simulated spectra with theory, one may conclude that the CH structure starts with a slightly higher effective k value, followed by a region of a reduced k value. The spectra are well comparable.

Moreover, to see the effect of the beta profile of the structure, a 30-cell structure with identical total length and the energy profile corresponding to the original cavity from Fig. 7 was simulated. It was found that the beta profile in that case has negligible influence on the mode spectrum (see Fig. 9).

Furthermore, the frequencies at the upper limit of the spectrum are well separated from the E_{010} mode, which is identified at 646.4 MHz.

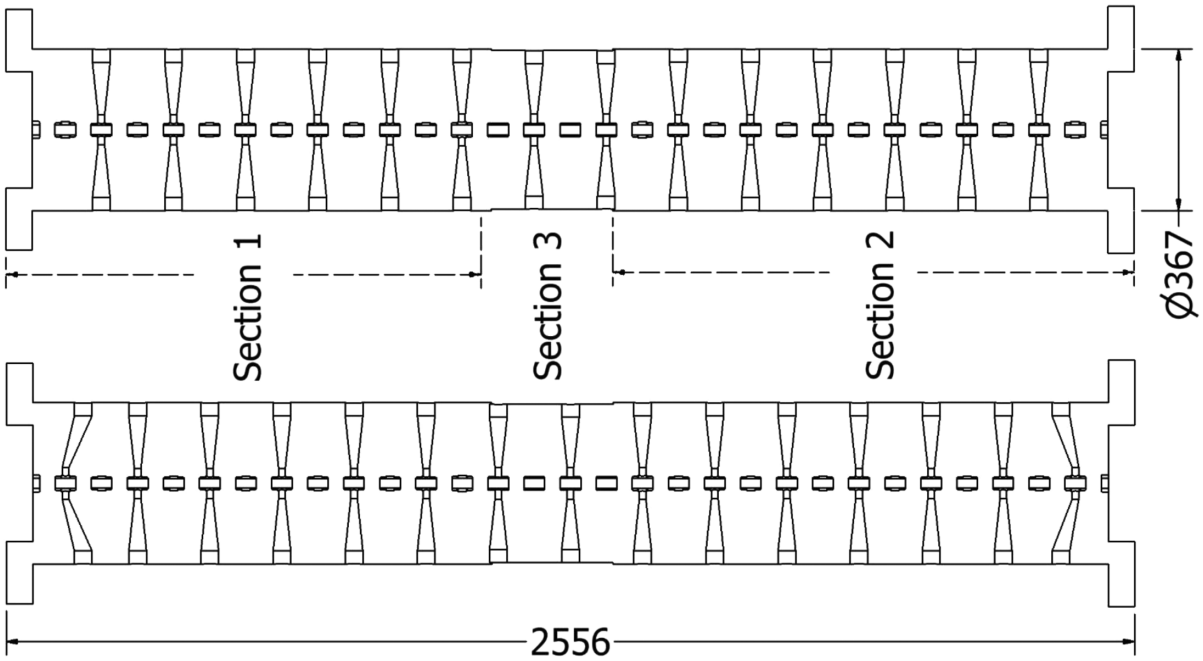

FIG. 8. Constant-beta CH cavity with 30 cells when replacing the coupling cell with four ordinary drift tubes.

The field and voltage distributions of the constant-beta 30-cell CH cavity in the zero mode are shown in Figs. 10–12.

B. CCH cavity configuration by insertion of the coupling cell

In the next step, the four drift tubes in section 3 are replaced by the lens housing, to get a CCH cavity. There are three options for how to orient the stems of the lens and the next-neighbor drift tubes. This is shown in Fig. 13. In the example discussed here with a lens of $2\beta\lambda$ in length, case B would be the natural choice by just removing the four drift tubes inserted before.

The effective gap voltages can be matched very well to the design values as given from beam dynamics calculations (Figs. 14 and 15). The coupling through the lens section can be tuned by the local cavity diameter at the lens—see Fig. 16 and Table VI.

The coupling section 3 oscillates in a $n\beta\lambda$ mode (Alverez mode) and couples sections 1 and 2 by magnetic fields around the lens as well as by the electric gap fields. The rf

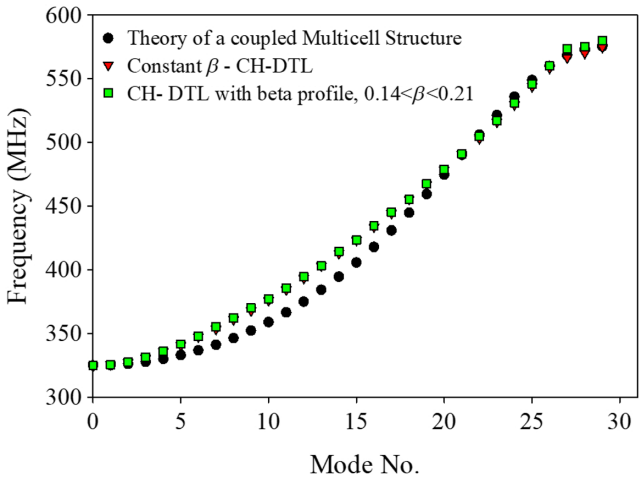

FIG. 9. Mode spectra for a 30-cell cavity according to Eq. (1), to simulations on a 30-cell CH cavity as shown in Fig. 8, and additionally for a CH cavity with a beta profile and identical total length.

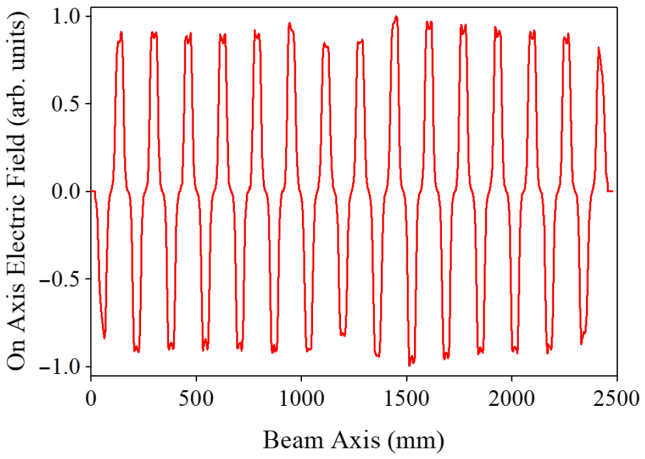

FIG. 10. On-axis electric field distribution along the tuned 30-cell CH cavity in the H_{210} mode.

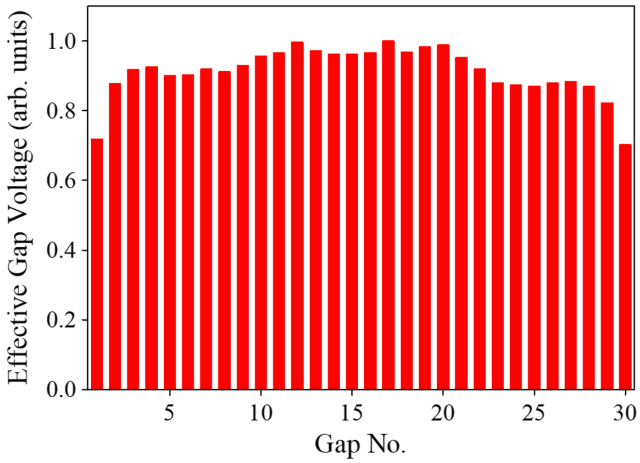

FIG. 11. Effective gap voltage distribution of the 30-cell CH cavity in the H_{210} mode.

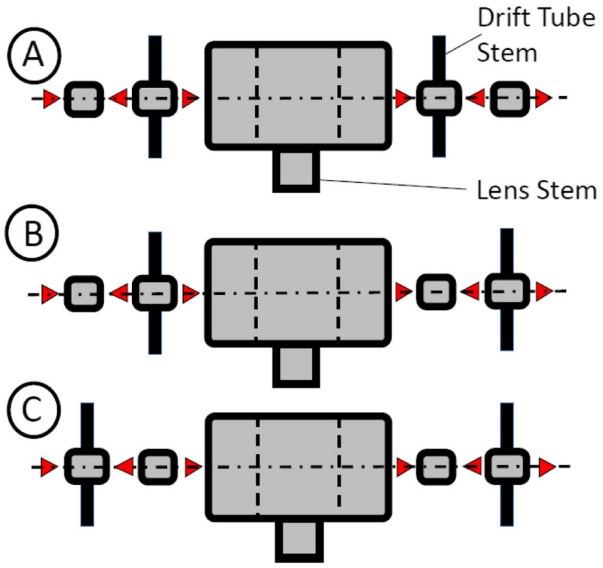

FIG. 13. Orientation of the stems around the lens: Three options are given, all of them resulting in a very similar behavior and mode spectrum. The gap E-field directions at one moment are indicated by red arrows.

currents oscillate along the central tube. This can be seen clearly in Figs. 17–19, where the magnetic field distributions within specified planes are displayed for cases A and B (Fig. 13). As a result, the stem of the coupling cell containing the quadrupole triplet carries no net rf current. This tube oscillates like in the E_{010} mode. The magnetic field flows from the quadrants of the accelerating sections into the coupling volume and forms a main H_θ component. Figure 18 shows the field distributions around the lens in the transverse $\overline{CC'}$ plane for coupling cases A (a) and B (b). Case A shows the highest field level around the lens stem, due to the vertical next-neighbor drift tube stem orientations—but at opposite rf potential. Case B shows field maxima in the horizontal plane due to the horizontal orientation of the next-neighbor drift tube stem (Fig. 19).

How the H_z fields in both CH sections are oriented relatively to each other depends on the orientation of the stem in front of the coupling cell and the stem after the coupling cell. The three options are illustrated in Fig. 13. The coupling lens acts as a magnetic field—combiner of the individual flows from the quadrants of sections 1 and 2: The stem arrays "case A" and "case C" lead to opposite magnetic field directions in corresponding quadrants from sections 1 and 2. Stem array "case B" instead results in identical magnetic field directions at corresponding quadrants. These three modes are considered "zero modes" for the three different geometries. The field distributions and resonance frequencies are very close to each other in identical tank shapes. The differences can be seen in Table VI.

The first higher mode is separated from the operating mode by at least 700 kHz, corresponding to 30 bandwidths of the unloaded cavity. The inductive feeder position can be chosen close to the cavity midplane where it does not couple to the second mode. As we see now from the shunt impedances, there is no real difference between all three configuration cases A–C. The Q value is higher for case C, as the losses on the lens stem are reduced due to lower magnetic surface fields, as soon as both nearest drift tube stems are out of the lens stem plane. However, the shunt impedance of the cavity does not profit. The advantage of

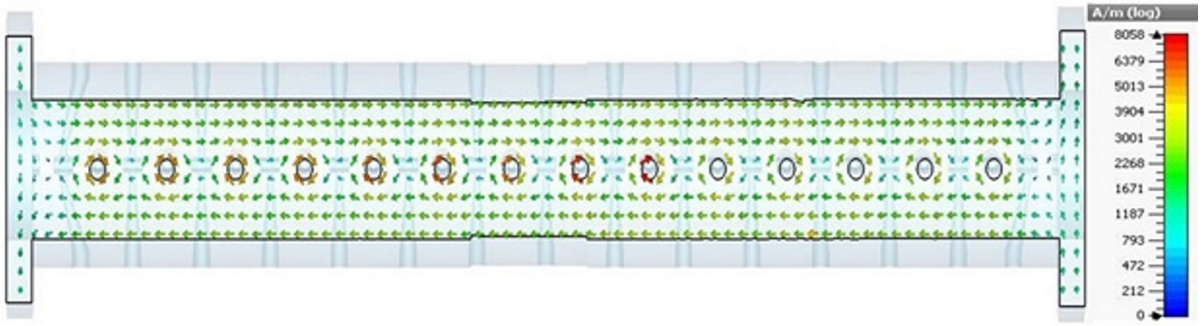

FIG. 12. Magnetic field distribution of the H_{210} mode in a horizontal plane above the beam axis as indicated in Fig. 18 by $\overline{AA'}$.

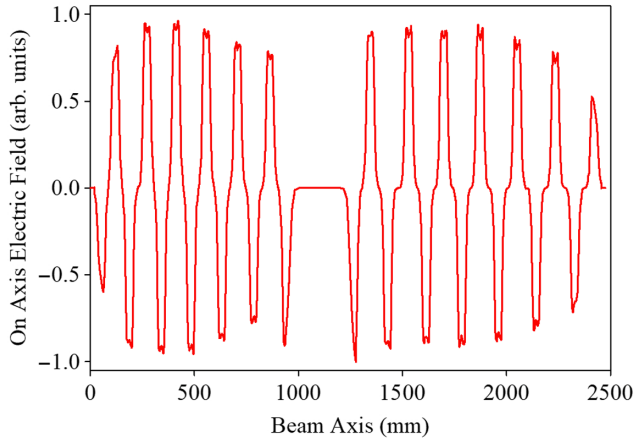

FIG. 14. Electric on-axis field distribution along the CCH cavity in zero mode. The stem array case A was chosen.

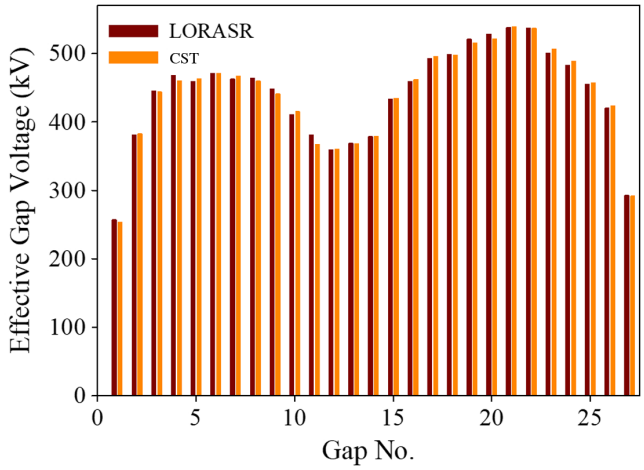

FIG. 15. Match between effective gap voltages as applied in beam dynamics and reached agreement by CST simulations on the electric field distribution. The central dip was achieved by a local reduction of the tank diameter to keep the gap fields at the large drift tube at modest values.

case A is the slightly larger tank diameter in section 3 around the coupling lens, due to the high magnetic field at the lens stem position, tuning the frequency up.

When an adequate number of ordinary drift tubes is removed from an H-type cavity and replaced by a lens containing a long drift tube, the reduction in effective shunt impedance for the cavity with internal lens (CCH structure) against the free lens CH structure can be estimated as follows:

The shunt impedance Z_0 is defined as

$$Z_0 = \frac{(\sum_{i=1}^{N} V_{i,0})^2}{\mathrm{Pl}}, \tag{7}$$

where $V_{i,0}$ is the gap voltage amplitude of gap i, P is the power loss along the structure of length l, and N is the total number of gaps.

Let us assume, N is the gap number of the CH structure with added gaps to replace the lens, and M is the number of drift tubes that are then removed and replaced by a lens containing a long drift tube. That means, $(M-1)$ gaps are missing now, while the length of the cavity was kept constant.

For a perfect zero mode, all gaps have equal voltage. Thus, the nominator and denominator of Eq. (7) will be changed by that procedure like

$$\left(\sum_{i=1}^{N} V_{i,0}\right)^2 \rightarrow \left(\sum_{i=1}^{N-M+1} V_{i,0}\right)^2 \tag{8a}$$

and

$$Pl \rightarrow \left(\frac{N-M+1}{N} + \frac{M-1}{N}\frac{\rho'}{\rho}\right) Pl\,. \tag{8b}$$

The surface resistance ratio ρ'/ρ expresses the ratio of power losses per unit length along a big drift tube in comparison with a conventional drift tube structure. This gives a reduction factor for the shunt impedance with an internal lens as

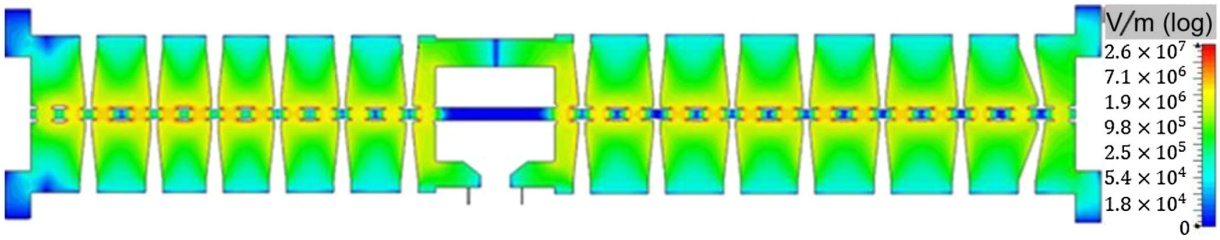

FIG. 16. Absolute electric field strength in the yz plane containing the beam axis, for stem array case A. The field concentration toward the aperture is clearly visible.

TABLE VI. Comparison between the four cavity geometries.

Cavity	Frequency zero mode (MHz)	Frequency $\pi/29$ mode (MHz)	Frequency $2\pi/29$ mode (MHz)	Quality factor Q	Shunt impedance for zero mode (MΩ/m)	Tank diameters per section, Ø (mm) Section 1/section 3/section 2
CCH A	324.621	325.352	328.187	13 895	53.2	363.8/349.0/370.2
CCH B	324.655	325.358	328.402	13 878	53.8	363.8/342.0/370.2
CCH C	324.408	325.220	327.733	14 244	53.2	363.8/342.0/370.2
CH, 30 cells	324.686	325.552	327.625	14 036	58.6	366.2/360.2/366.6

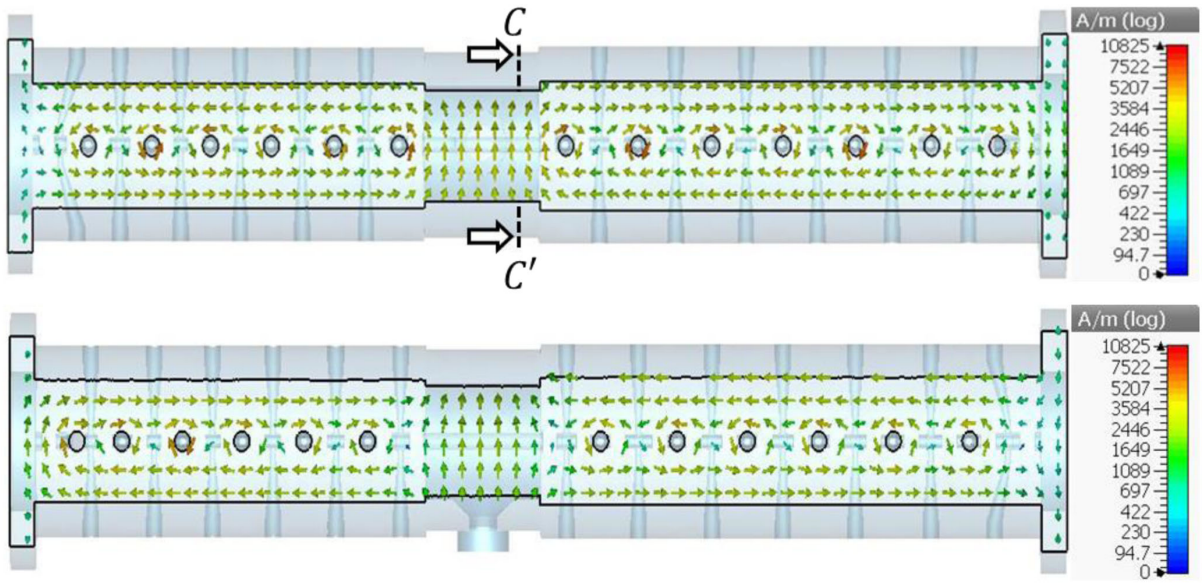

FIG. 17. Magnetic field distributions in $\overline{AA'}$ and $\overline{BB'}$ planes as indicated in Fig. 18, for stem array case A.

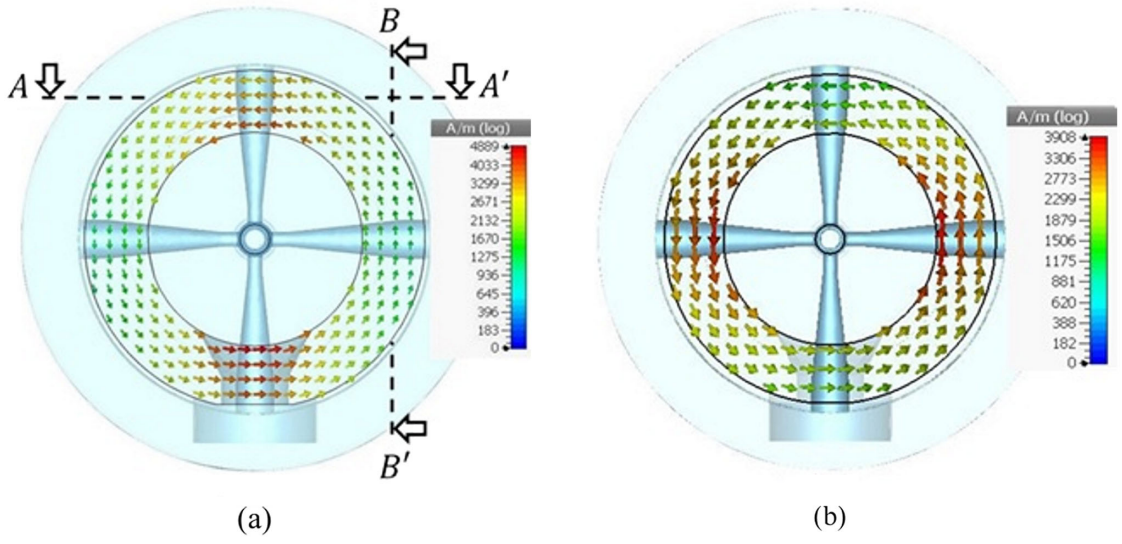

FIG. 18. Cross-sectional views $\overline{CC'}$ of the magnetic field distributions in the coupling cell close to the lens stem for stem array case A (a) and for stem array case B (b).

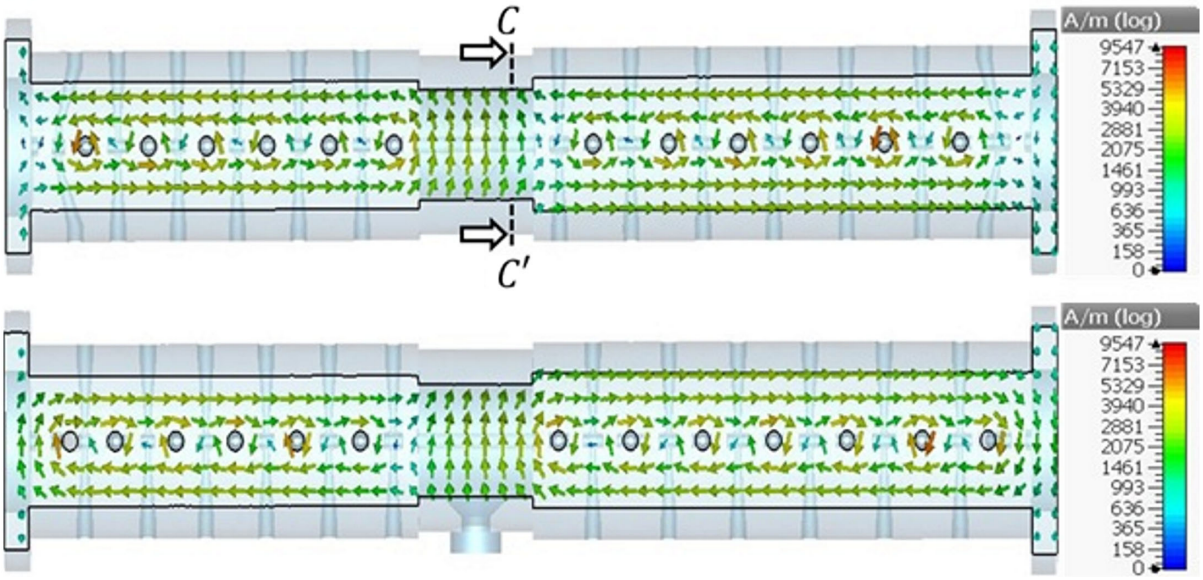

FIG. 19. Magnetic field distributions in $\overline{AA'}$ and $\overline{BB'}$ planes as indicated in Fig. 18, for stem array case B.

$$F_s = \frac{(N-M+1)^2}{N^2}\left(\frac{N-M+1}{N} + \frac{M-1}{N}\frac{\rho'}{\rho}\right)^{-1}. \quad (9)$$

In the best case, we can assume, that the losses along the big lens are very small, which means $\frac{\rho'}{\rho} \to 0$. In that optimistic case, one gets

$$F_s = \frac{(N-M+1)^2}{N^2}\left(\frac{N-M+1}{N}\right)^{-1} = \frac{N-M+1}{N}. \quad (10)$$

In our study, $N = 30$ and $M = 4$ resulting in $F_s = 0.9$. That means, the shunt impedance for the 30-cell structure has to be at least 10% higher than all other cases with a lens, and this is in good agreement with the rf simulations as shown in Table VI. The effective shunt impedance Z_{eff} is received from Eq. (7) by multiplying each gap voltage $V_{i,0}$ by the transit time factor T_i. As the transit time factors are higher for the shorter gaps in the end regions of CH cavities, it may additionally support a relatively small effect of the lens insertion on the shunt impedance.

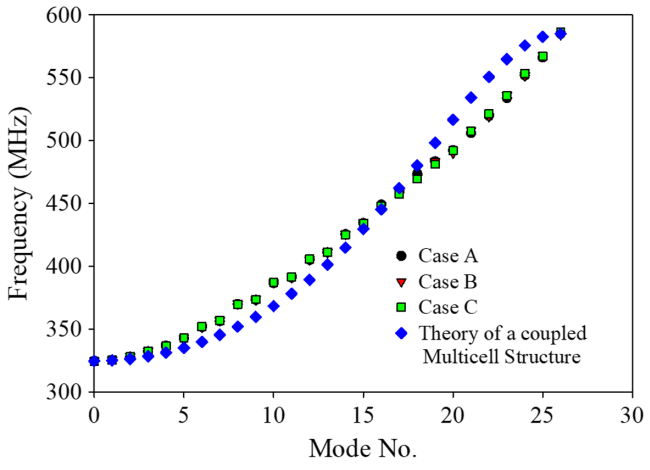

FIG. 20. 27-cell mode spectrum and comparison with the simulated mode—spectra for the three CCH—options A, B, and C as explained in Fig. 13.

Finally, the mode spectrum of the three CCH options is shown in Fig. 20 together with a 27-cell spectrum according to Eq. (2).

In conclusion, all three cases A, B, and C are fine for realization. A final choice among them can be made due to cooling or mechanical aspects.

IV. CONCLUSIONS

The standard concept to flatten the voltage distribution along H-type cavities is undercuts (in the vane ends in case of four-vane RFQs or in the girders carrying the drift tubes in case of IH- or CH-DTLs). Alternatively, one can locally extend the tank diameter and use inclined stems at the cavity ends. This is especially useful if there are no girders used and the stems are directly connected to the cavity walls. The main geometric parameters were identified and their influence was described for a typical design example.

In case of four-vane RFQs, the cavity end geometry with an extended tank diameter might be attractive in the case of production techniques that are in favor of avoiding undercuts—like additive manufacturing or water-cooling problems.

It was shown, that the tuning and higher mode characteristics are very similar for an ordinary CH cavity when compared to a CCH cavity by replacing the coupling cell with an adequate number of ordinary drift tubes. The CH cavity can be designed and tuned by simulations much

faster. In the final step, one can just replace the drift tubes along the envisaged $n\beta\lambda$ long lens section with the coupling cell. Tuning is then achieved by only a minor final variation of the local tank diameter at the coupling cell.

The rf simulations show that the effective shunt impedance only lowers by around 10% after the integration of one coupling cell with length 2 beta lambda into a CH cavity with about 30 cells. This coupling method allows, therefore, efficient use of identical, powerful klystron amplifiers and a one-to-one match between the amplifier and cavity along the linac, starting with beam energies at 3 MeV or above from an RFQ.

ACKNOWLEDGMENTS

Supported by GU-GSI F&E Funds 2017–2019, Helmholtzzentrum für Schwerionenforschung, Darmstadt, Germany.

[1] T. Wangler, *RF Linear Accelerators*, 2nd ed. (Wiley-VCH Verlag GmbH & Co. KGaA, Weinheim, 2008).

[2] U. Ratzinger, H. Hähnel, R. Tiede, J. Kaiser, and A. Almomani, Combined zero-degree structure beam dynamics and applications, Phys. Rev. Accel. Beams **22**, 114801 (2019).

[3] G. Clemente *et al.*, Development of room temperature crossbar-H-mode cavities for proton and ion acceleration in the low to medium beta range, Phys. Rev. ST Accel. Beams **14**, 110101 (2011).

[4] C. M. Kleffner *et al.*, Status of the FAIR proton linac, in *Proceedings of the 10th International Particle Accelerator Conference, IPAC-2019, Melbourne, Australia* (JACoW, Geneva, Switzerland, 2019), 10.18429/JACoW-IPAC2019-MOPTS020.

[5] D. Mäder *et al.*, Status and development of the MYRRHA injector, in *Proceedings of the 9th International Particle Accelerator Conference, IPAC-2018, Vancouver, Canada* (JACoW, Geneva, Switzerland, 2018), 10.18429/JACoW-IPAC2018-MOPML017.

[6] J. H. Billen, L. M. Young, S. Kurrenoy, and K. R. Crandall, Room-temperature Linac structures for the Spallation Neutron Source, in *Proceedings of the 19th Particle Accelerator Conference, Chicago, IL, 2001* (IEEE, Piscataway, NJ, 2001).

[7] L. Arnoudon *et al.*, Linac4 Technical Design Report, edited by F. Gerigk and M. Vretenar, European organization for nuclear research CERN—AB department, Geneva, Switzerland, Report No. CERN-AB-2006-084 ABP/RF, 2006.

[8] F. Grespan, M. Comunian, A. Pisent, M. Poggi, and C. Roncolato, ESS DTL design and drift tube prototypes, in *Proceedings of 27th Linear Accelerator Conference, LINAC2014, Geneva, Switzerland* (JACoW, Geneva, Switzerland, 2014).

[9] J. Broere *et al.*, High power conditioning of the 202 MHz IH Tank 2 at the CERN LINAC3, in *Proceedings of the 19th International Linear Accelerators Conference, Chicago, IL, 1998* (NTIS, Springfield, VA, 1998), p. 771.

[10] M. Maier *et al.*, Commissioning of the linac for the Heidelberg Heavy Ion Cancer Therapy Centre (HIT), in *Proceedings of the 22nd Particle Accelerator Conference, PAC-2007, Albuquerque, NM* (IEEE, New York, 2007), THPMN014, pp. 2734–2736.

[11] U. Ratzinger, A low beta rf linac-structure of the IH-type with improved radial acceptance, in *Proceedings of the 1988 Linear Accelerator Conference, LINAC-1988, Newport News, VA* (JACoW, Geneva, Switzerland, 2003), p. 185.

[12] Matthew J. Easton, Haipeng Li, Yuanrong Lu, Jie Zhu, and Pierre-Daniel Pfister, Permanent-magnet quadrupoles for an interdigital H-mode drift tube linear accelerator: Optimization code and adjustable magnet design, Phys. Rev. Accel. Beams **21**, 122401 (2018).

[13] S. S. Kurennoy, L. J. Rybarcyk, J. F. O'Hara, E. R. Olivas, and T. P. Wangler, H-mode accelerating structures with permanent-magnet quadrupole beam focusing, Phys. Rev. ST Accel. Beams **15**, 090101 (2012).

[14] G. Schreiber, E. Plechov, J. Salvatore, B. Schlitt, A. Schnase, and M. Vossberg, First high power tests at the 325 MHz RF test stand at GSI, in *Proceedings of the 28th Linear Accelerator Conf. (LINAC'16), East Lansing, MI, 2016*, MOPLR067, pp. 287–289, 10.18429/JACoW-LINAC2016-MOPLR067.

[15] U. Ratzinger, H-type linac structures, in *Proceedings of CAS CERN Accelerator School, Radio Frequency Engineering, Seeheim, Germany* (CERN, Geneva, 2000), pp. 351–379.

[16] M. Otani *et al.*, APF IH-DTL design for the Muon Linac in the J-PARC Muon G-2/EDM Experiment, in *Proceedings of the 7th International Particle Accelerator Conference, IPAC-2016, Busan, Korea* (JACoW, Geneva, Switzerland, 2016), pp. 1539–1542, 10.18429/JACoW-IPAC2016-TUPMY002.

[17] H. Hähnel, A. Ates, B. Dedic, and U. Ratzinger, Additive manufacturing of an IH-type linac structure from stainless steel and pure copper, Instruments **7**, 22 (2023).

[18] A. Seibel *et al.*, Welding and copper plating investigations on the FAIR Proton Linac, in *Proceedings of 31st International Linear Accelerator Conference, LINAC-2022, Liverpool, UK* (JACoW, Geneva, Switzerland, 2022), pp. 345–347, 10.18429/JACoW-LINAC2022-TUPOJO05.

[19] U. Ratzinger, The New High Current Ion Accelerator at GSI and perspectives for linac design based on H-mode cavities, in *Proceedings of the 7th European Particle Accelerator Conference, Vienna, Austria, 2000* (EPS, Geneva, 2000).

[20] A. Almomani and U. Ratzinger, Status of a 325 MHz high gradient CH cavity, in *Proceedings of 28th Linear Accelerator Conference, LINAC-2016, East Lansing, MI* (JACoW, Geneva, Switzerland, 2016), THPLR059, pp. 982–984, 10.18429/JACoW-LINAC2016-THPLR059.

[21] J. P. Carneiro, B. Mustapha, and P.N. Ostroumov, Beam physics of the 8-GeV H-linac, Nucl. Instrum. Methods Phys. Res., Sect. A **606**, 271 (2009).

[22] S. S. Kurennoy *et al.*, An H-mode accelerator with PMQ focusing as a LANSCE DTL replacement, in *Proceedings of the 2nd International Particle Accelerator Conference, IPAC-2011, San Sebastián, Spain* (EPS-AG, Spain, 2011).

[23] R. Brodhage, W. Vinzenz, G. Clemente, and U. Ratzinger, First coupled CH power cavity for the FAIR Proton Injector, in *Proceedings of the 5th International Particle Accelerator Conference, IPAC-2014, Dresden, Germany* (EPS-AG, Dresden, 2014), pp. 3232–3234, 10.18429/JACoW-IPAC2014-THPME011.

[24] CST Studio Suite, https://www.3ds.com/products/simulia/cst-studio-suite.

[25] A. Almomani *et al.*, Updated cavities design for the FAIR p-linac, J. Phys. Conf. Ser. **874**, 012046 (2017).

[26] M. Mayerhofer *et al.*, Additive manufactured coupled cavity linac structures from pure copper, Instruments **7**, 56 (2023).

[27] T. Torims *et al.*, Evaluation of geometrical precision and surface roughness quality for the additively manufactured radio frequency quadrupole prototype, in *Proceedings of the 13th International Particle Accelerator Conference, IPAC-2022, Bangkok, Thailand* (JACoW, Geneva, Switzerland, 2022), pp. 787–791, 10.18429/JACoW-IPAC2022-TUOXSP3.